

# Micrometer and Nanometer Scale Photopatterning of Proteins on Glass Surfaces by Photo-degradation of Films Formed from Oligo(Ethylene Glycol) Terminated Silanes

Getachew Tizazu · Osama el Zubir · Samson Patole · Anna McLaren · Cvetelin Vasilev · David J. Mothersole · Ali Adawi · C. Neil Hunter · David G. Lidzey · Gabriel P. Lopez · Graham J. Leggett

Received: 28 June 2012 / Accepted: 10 August 2012 / Published online: 5 September 2012  
© The Author(s) 2012. This article is published with open access at Springerlink.com

**Abstract** Exposure of films formed by the adsorption of oligo(ethylene glycol) (OEG) functionalized trichlorosilanes on glass to UV light from a frequency-doubled argon ion laser (244 nm) causes photodegradation of the OEG chain. Although the rate of degradation is substantially slower than for monolayers of OEG terminated thiolates on gold, it is nevertheless possible to form micrometer-scale patterns by elective adsorption of streptavidin to exposed regions. A low density of aldehyde functional groups is produced, and this enables derivatization with nitrilotriacetic acid via an amine linker. Complexation with nickel enables the site-specific immobilization of histidine-tagged yellow and green fluorescent proteins. Nanometer-scale patterns may be fabricated using a Lloyd's mirror interferometer, with a sample and mirror set at right angles to each other. At low exposures, partial degradation of the OEG chains does not remove the protein-resistance of the surface, even though friction force microscopy reveals the formation of patterns. At an exposure of ca.  $18 \text{ J cm}^{-2}$ ,

the modified regions became adhesive to proteins in a narrow region ca. 30 nm ( $\lambda/8$ ) wide. As the exposure is increased further the lines quickly broaden to ca. 90 nm. Adjustment of the angle between the sample and mirror enables the fabrication of lines of His-tagged green fluorescent protein at a period of 340 nm that could be resolved using a confocal microscope.

## 1 Introduction

Protein patterning is important in many applications, from fundamental studies of cellular interactions [1–7], molecular recognition [8], and other phenomena, to the development of biosensors for the detection and diagnosis of disease [9, 10]. However, the control of the spatial organization of proteins remains challenging. The greater part of the literature on bionanofabrication has addressed the patterning of oligonucleotides [11–13], and there is much less work that has addressed the fabrication of protein nanostructures [14–23]. Similarly, while there is a mature market for chip-based DNA analysis systems, the protein chip remains at a very early stage of development. Undoubtedly, the significant difficulties associated with the formation of protein patterns are an important factor in both cases. Proteins can explore large conformational spaces, so they adhere strongly to most surfaces. This renders both spatial and orientational control of adsorption difficult because, proteins may adhere to regions, where they are not required and because, they may become kinetically trapped in an unfavorable orientation, even where a linking group is available at the surface to promote site-specific attachment. Moreover, proteins can undergo facile conformational change after adsorption to surfaces, rendering control of conformation difficult.

---

G. Tizazu · O. el Zubir · S. Patole · A. McLaren · D. J. Mothersole · G. J. Leggett (✉)  
Department of Chemistry, University of Sheffield,  
Brook Hill, Sheffield S3 7HF, UK  
e-mail: Graham.Leggett@sheffield.ac.uk

S. Patole · C. Vasilev · C. N. Hunter  
Department of Molecular Biology and Biotechnology,  
University of Sheffield, Western Bank, Sheffield S10 2TN, UK

A. Adawi · D. G. Lidzey  
Department of Physics and Astronomy, University of Sheffield,  
Hounsfield Road, Sheffield S3 7RH, UK

G. P. Lopez  
Department of Biomedical Engineering, Duke University,  
Durham, NC 27708, USA

The most important challenge in organizing proteins at interfaces is the control of non-specific adsorption. The most widely reported approaches employ poly(ethylene glycol) [24] and oligomeric ethylene glycol [1, 2, 25–27], and related materials such as oligo(ethylene glycol) (OEG) methacrylate brushes [28–30] and plasma-polymerized tetraglyme [31]. However, there is a growing group of other materials, such as zwitterionic poly(methacryl phosphorylcholine) brushes [32–35], that have also been found to exhibit strong resistance to non-specific adsorption. Self-assembled monolayers of OEG terminated alkylthiolates adsorbed on gold surfaces are exceptionally resistant to protein adsorption, and have been used previously to fabricate protein patterns [1–3]. They are conveniently patterned by a variety of methods, including micro-contact printing [1, 2] and, at smaller length-scales, dip-pen nanolithography [5], near-field lithography [18, 20, 36, 37], electron beam lithography [38–40], and nanoimprinting [21]. However, gold has a marked propensity to quench fluorescence, and attenuates transmitted light. Given the significance of optical methods for the characterization of biological systems, these are significant limitations. Glass is a very important substrate for biologists, but comparatively speaking, much less attention has been given to the precise patterning of proteins on glass surfaces [20].

Oligo(ethylene glycol) materials have been demonstrated previously to be susceptible to photodegradation at 244 nm. Ducker et al. [36] found that triethylene glycol functionalized SAMs of alkylthiolates on gold were rapidly degraded by UV exposure to yield protein-binding aldehyde functional groups. Subsequently, plasma-polymerized tetraglyme [41], poly(oligoethylene methacrylate) polymer brushes [42] and monolayers [20, 43] have been modified by photodegradation, to facilitate protein patterning. In this paper, we present a simple method for patterning proteins on glass, based on spatially selective photodegradation of a protein-resistant film formed by the adsorption of 2-[methoxy(polyethylenoxy)propyl] trichlorosilanes to yield protein-binding regions. Films of this adsorbate have been patterned previously using conventional photolithography involving exposure and development of a photoresist [44]; here we demonstrate direct patterning by photodegradation and also the fabrication of nanometer scale patterns by interferometric lithography. The use of processes that do not require photoresist is likely to be important in the development of strategies for the fabrication of multicomponent protein nanopatterns redeposition and development of photoresist in successive steps would damage proteins attached to the surface. Thus, there is a need for simple methods that involve direct conversion of protein-resistant materials to protein-binding ones.

At the nanometer scale, protein patterning remains challenging. Moreover, there is also an urgent need for methods that enable control of biomolecular organization

at high resolution over macroscopic areas [15, 17]. Previously, successful approaches to patterning over large areas have included the use of self-assembling arrays of polymer-stabilized metal nanoparticles [16], and micro-contact printing [17]. Here, we report an alternative approach that is compatible with the rapid patterning of large areas. In interferometric lithography (IL) [45–48], two or more coherent laser beams interfere to produce a periodic intensity pattern that is used to expose a photosensitive material. The interference pattern has a period  $\lambda/2n\sin\theta$ , where  $\lambda$  is the wavelength of the excitation beam,  $n$  is the refractive index of the medium and  $2\theta$  is the angle between the two interfering beams. The exposure process is rapid and by changing the geometry and number of interfering laser beams, it is possible to change quickly and readily the nature of the resulting interference pattern. Macroscopic areas may be exposed in a maskless process using, other than a UV laser, only very simple apparatus. The method is potentially very attractive for many laboratories that do not possess extensive infrastructure for nanofabrication. As an example, we demonstrate herein the fabrication of 30 nm lines of streptavidin at a period of 180 nm over a region ca. 1 cm<sup>2</sup> in area.

## 2 Experimental

All glassware and substrates were cleaned before using piranha solution [a mixture of 30 % H<sub>2</sub>O<sub>2</sub> and 98 % concentration sulfuric acid (both purchased from Fisher Scientific, Loughborough, UK)] in the ratio 3:7 for 45 min. (Caution: piranha solution is a strong oxidizing agent and has been known to detonate spontaneously upon contact with organic material; it should be handled with extreme caution). After treatment with piranha solution, glassware, and substrates were rinsed with copious amounts of deionized water (Elga Pure Nanopore, 18.2 MΩ) and dried in an oven. Silane films were formed by immersing clean substrates in a 1 mmol dm<sup>-3</sup> solution of 2-[methoxy(polyethylenoxy)propyl] trichlorosilane (OEG-silane), CH<sub>3</sub>O(C<sub>2</sub>H<sub>4</sub>O)<sub>6-9</sub>(CH<sub>2</sub>)<sub>3</sub>Cl<sub>3</sub>Si (Gelest, Maidstone, UK), henceforth OEG-silane, in dry toluene under nitrogen.

The gene sequence of yellow fluorescent protein (YFP) was amplified by PCR from pCS2-Venus vector (a kind gift from Dr. Atsushi Miyawaki, RIKEN Brain Science Institute, Japan). The resulting Nde I/Bam HI fragment was cloned into a pET14b expression vector (Novagen). Introducing the combined F64L, S65T, V68L, S72A, M153T, V163A, S175G, and A206K mutations into the YFP gene resulted in enhanced green fluorescent protein (GFP) gene [49]. Both His<sub>6</sub>-YFP and His<sub>6</sub>-GFP proteins were produced by heterologous expression in *E. coli* (BL21); cells were grown to an O.D<sub>680</sub> of 0.6 at 37 °C then induced using

IPTG (0.4 mM) for 12 h at 25 °C. Pelleted cells (19,000×g/20 min) were lysed by sonication, and the resulting lysate was clarified by a further spin (33,000×g/30 min). Both His-tagged fluorescent proteins were purified to homogeneity from clarified lysate using a Chelating Sepharose Fast Flow Ni-NTA gravity flow column (GE Healthcare) as detailed in the manufacturer's instructions. Protein purity was assessed by gel electrophoresis (SDS-PAGE).

Alexa Fluor 647-conjugated streptavidin and Fluospheres<sup>®</sup> NeutrAvidin<sup>®</sup> labeled particles, 0.04 μm, yellow-green fluorescent (505/515) 1 % were purchased from Invitrogen, Paisley, UK. Both were dissolved in 0.1 M PBS at a concentration of 10 μg mL<sup>-1</sup>. The samples were immersed in these solutions for 2 h, washed with PBS solution and deionized water and gently dried with nitrogen, before being characterized using confocal microscopy.

Photopatterning was carried out using a Coherent Innova 300C FreD frequency-doubled argon ion laser (Coherent UK, Ely, UK), emitting at 244 nm with a maximum power of 100 mW. The beam was expanded using a divergent lens to irradiate an area ca. 0.8 cm in diameter. Micrometer-scale patterns were fabricated by exposing the sample through an electron microscope grid (Agar, Cambridge, UK).

Surface analysis by X-ray photoelectron spectroscopy (XPS) was carried out using a Kratos Axis Ultra X-ray photoelectron spectrometer (Kratos, Manchester, UK), equipped with a monochromatic Al-K $\alpha$  X-ray source operating with a base pressure of 10<sup>-10</sup> mbar. For high resolution scans, an electron energy analyzer pass energy of 80 eV was used. Data were processed using CasaXPS software (<http://www.casaxps.com/>). All binding energies were referenced to the main hydrocarbon peak, set at a binding energy of 285 eV. Peaks were fitted with a linear background, using symmetrical Voigt type functions, with contributions from both Gaussian and Lorentzian profiles (typically in the proportion 90 % Gaussian to 10 % Lorentzian). The full width at half maximum (FWHM) values of the peaks within a given spectrum were constrained to be identical and were found to be 1.31 ± 0.02 eV. Contact mode topographical and friction imaging and tapping mode characterization were performed using a Multimode atomic force microscope with a Nanoscope IIIA controller (Veeco, Santa Barbara, USA). Silicon nitride probes with nominal spring constants of 0.06 and 0.12 Nm<sup>-1</sup>, and tip radii of between 20 and 60 nm (Veeco), were used for contact mode measurements. For tapping mode, Si probes (Veeco, TESP) were used.

Fluorescence images of the His-tagged GFP and YFP patterns were obtained on a Delta Vision RT Microscope (Applied Precision, Issaquah, WA). The samples were placed on a microscope slides followed by a mount in

Citifluor as an antifade reagent (glycerol-PBS solution, AF1) (Citifluor Ltd., London, United Kingdom). A 60× UPLSAPO magnification oil immersion lens with a numerical aperture of 1.42 was used for imaging. A small drop of immersion oil (Type F, Olympus) was placed on the slide in the center of the illuminated area. A bandpass filter (FITC Ex-490/20) was used to excite the GFP on the surface and the fluorescence was collected with band pass emission filter (FITC Em-528/38). The fluorescence images were analyzed using Image J version 1.46J image processing software.

### 3 Results and Discussion

#### 3.1 UV Photodegradation

Films formed by the adsorption of 2-[methoxy(polyethylenoxy)propyl] trichlorosilane (OEG-silane), CH<sub>3</sub>O (C<sub>2</sub>H<sub>4</sub>O)<sub>6-9</sub>(CH<sub>2</sub>)<sub>3</sub>Cl<sub>3</sub>Si, on glass were exposed to UV light (244 nm) and characterized by XPS. Figure 1 shows a series of XPS C1s spectra acquired at increasing exposure. For the virgin film, a strong peak was observed at 286.7 eV, corresponding to the ether carbon atoms. Smaller peaks were also observed at 285.0 eV (C-C) and also at 289.3 eV (O-C=O). The origin of the latter peak is not clear; it possibly results from low levels of contamination from the atmosphere, due to the high surface energy (advancing water contact angle ca. 45°) of the OEG-silane film.

Following exposure to UV light, the most noticeable change in the C1s spectrum was a substantial decrease in the size of the ether component. This was attributed to degradation of the OEG group. The total area of the C1s peak envelope was found to have reduced, too, consistent with the removal of material from the surface. A very small peak was observed at ca. 288 eV, corresponding to an aldehydic carbon atom. These changes are consistent with photodegradation of the OEG group, and are qualitatively similar to those observed by Ducker et al. [36] in studies of OEG-terminated alkylthiolate SAMs on gold.

However, in quantitative terms, the behavior of the films on gold and glass was rather different. Figure 2 shows the variation in the relative intensity ratios as a function of the UV dose. As the exposure increased, the ether components of the C1s spectrum declined in intensity for OEG-containing SAMs formed on glass. The C1s peaks also declined in intensity and peak area, but the intensities of the ether components decreased relative to the total C1s area. The area of the aldehyde components remained approximately constant. The rate of decrease in the peak area of the ether component was much slower than that observed by Adams et al. [50] in a previous study of the

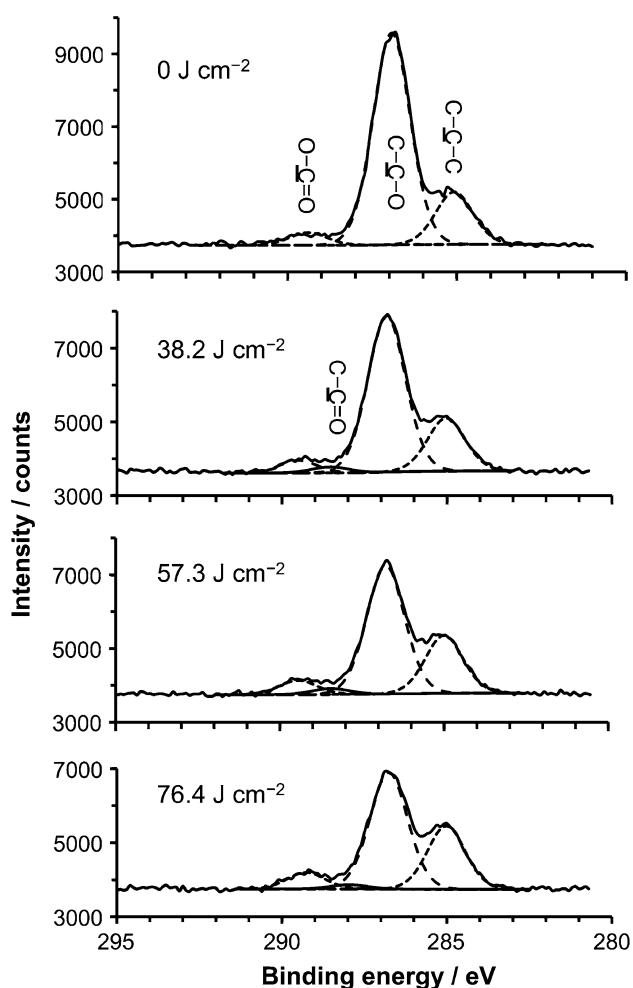


**Fig. 1** Change in the C1s region of the XPS spectrum of OEG-silane with UV exposure

photodegradation of triethylene glycol functionalized alkylthiolates SAMs on gold. Their data are also shown in Fig. 2. After an exposure of  $115 \text{ J cm}^{-2}$ , the  $\text{C-C-O}/\text{C-C-O}-\text{C}$  ratio measured for films of OEG-silane on glass is similar to the value measured for triethylene glycol terminated SAMs on gold after 1 % of this exposure. The relative area of the aldehyde component at an exposure of  $115 \text{ J cm}^{-2}$  was smaller, by a factor of ca. 3, than observed by Adams et al. for OEG-terminated SAMs on gold. The OEG-silane used here was not monodispersed, containing 6–9 ethylene glycol units per adsorbate molecule. Consequently, if photodegradation yielded the same number of intensity of the aldehyde component may simply reflect attenuation of the photoelectron signal by the longer OEG group in the OEG-silane film. Moreover, silane films are rarely monolayers; bilayers or thicker films are common. Ellipsometry yielded a mean thickness of  $1.6 \pm 0.2 \text{ nm}$  in the present case, indicating that multilayers were not formed; however, the film was unlikely to be completely uniform. The fact that the  $\text{C-C-O}/\text{C1s}$  ratio does not

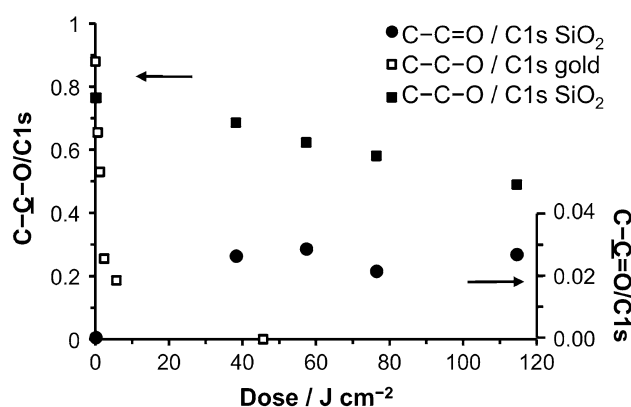


**Fig. 2** Variation in XPS intensity ratios with UV exposure for OEG-silanes on glass (*filled symbols*) and OEG terminated SAMs on gold [50] (*open symbols*)

approach zero may reflect the fact that in places an underlayer of molecular material lies beneath the surface and is unmodified even at comparatively large exposures.

These data, taken together, suggest that the degradation process for the OEG-silane films is qualitatively similar to that which occurs for OEG-terminated SAMs on gold, but that the rate of change is significantly smaller for the OEG-silane films. The reason for this is not clear. It has previously been suggested that hot electron formation at gold surfaces triggers the photo-oxidation of alkylthiolate SAMs during exposure to UV light [51, 52]; it is possible that hot electrons also accelerate degradative processes in the OEG chain. An alternative explanation is that the different optical properties of silicon dioxide, compared to gold, lead to an altered rate of modification.

### 3.2 Surface Patterning

Although, the rate of modification of the OEG-silane film was smaller than that of OEG-functionalized alkylthiolate SAMs on Au, it was still adequate to enable surface patterning to be carried out. After large exposures, measurable erosion of the surface film was observed. For example, Fig. 3a shows an AFM topographical image acquired in contact mode after an exposure of  $60 \text{ J cm}^{-2}$  through an electron microscope grid mask. The mean line section (averaged across a large number of lines in Fig. 3a shown underneath the image indicates that ca. 2.6 nm of material has been removed. This compares with the figure of 2.9 nm reported by Shah et al. [44] for complete removal of the adsorbate layer by conventional photolithography. This is larger than the estimate of the film thickness by ellipsometry, quoted above. A similar discrepancy was also reported by Shah et al. [53] in another work, where a thickness of ca. 2 nm was reported. One possible explanation for the discrepancy between the two figures is that the silane film



is not ideally close-packed; a reduction in the packing density may yield a reduced ellipsometric thickness.

Figure 3b shows a friction force microscopy (FFM) image acquired simultaneously with the topographical image in Fig. 3a. The exposed regions (squares) exhibit brighter contrast than the masked regions (bars), indicating that photodegradation causes an increase in the friction force measured by the probe and hence a larger coefficient of friction. The frictional interaction between the probe and the surface results from both adhesive contributions (shearing) and conformational changes induced by the interaction of the AFM probe with the surface under loading (molecular plowing). Contributions to friction from both shearing and plowing are likely to be increased following degradation of the surface, the creation of new oxygen-containing functional groups will lead to increased adhesion, and the degradation of the OEG chains will increase the degree of variation in chain length thus creating a less closely packed surface expected to deform more easily under loading. Both mechanisms are expected to lead to an increase in energy dissipation at the tip-sample contact and an increase in the coefficient of friction. However, it is notable that the contrast difference between the exposed and masked regions in Fig. 3 is quite clear, under conditions that yield only modest changes in the surface composition as determined by XPS. This suggests that the dominant effect on the friction force may be the change in molecular organization, rather than the change in composition (i.e., that it may result largely from the change in the relative contribution from shearing following photodegradation).

The extent of photomodification was monitored using FFM. The difference in the lateral photodetector signal

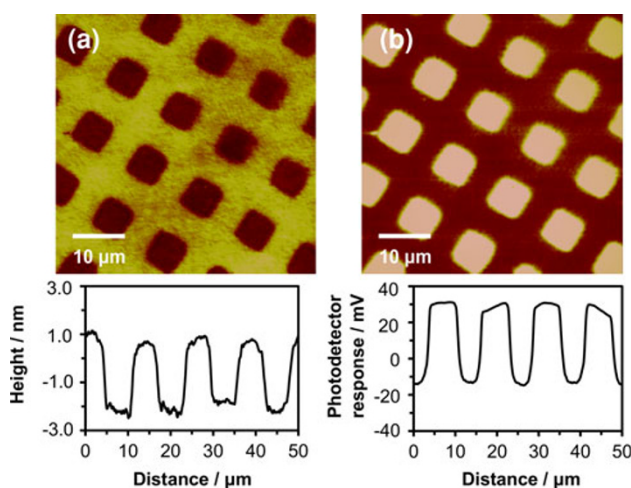


**Fig. 3** **a** AFM topographical image and **b** friction force microscopy image of a sample of OEG-silane following UV exposure through an electron microscope grid mask at  $60 \text{ J cm}^{-2}$ , together with averaged line sections

between the masked and exposed regions was measured from line sections through patterned samples, and is shown as a function of the exposure in Fig. 4. As the exposure increased, the magnitude of the difference in the friction signal between the masked and the exposed areas increased, mirroring the decline in the area of the ether peak in the C1s region. The value of the coefficient of friction measured at  $80 \text{ J cm}^{-2}$  is likely anomalously high; certainly it has a larger error bar than was measured at the largest exposure used. These data suggest that the limiting value of the coefficient of friction is achieved at an exposure in the range  $80\text{--}100 \text{ J cm}^{-2}$ . A similar study was carried out previously for poly(oligoethylene methacrylate) polymer brushes. A limiting coefficient of friction was measured for these materials after an exposure of only  $2 \text{ J cm}^{-2}$ , indicating a much faster rate of degradation than was observed for the silane films studied here.

Micropatterned samples were immersed in solutions of Neutravidin particles, which are avidin-coated, dye-labeled polymer nanoparticles. Figure 5a shows a fluorescence microscopy image of a pattern prepared by exposure of an OEG-silane film to UV light through a mask. Bright contrast is observed from regions that were exposed to UV light (the squares), while dark contrast is observed from regions that were masked during exposure (the bars). The contrast difference is clear, with few spots of fluorescence on the bars, indicating that there is very little non-specific adsorption onto the unmodified regions. In contrast, in the exposed regions, the degradation of the OEG chains enables adsorption of the protein-coated particles. Figure 5b shows a tapping mode AFM topographical image of a similar sample. There is clear height contrast between the exposed and masked regions, consistent with the fluorescence image. Figure 5c shows a sample that has been exposed to UV light through a mask and immersed in a solution of Alexa Fluor 532-labeled streptavidin. Clear

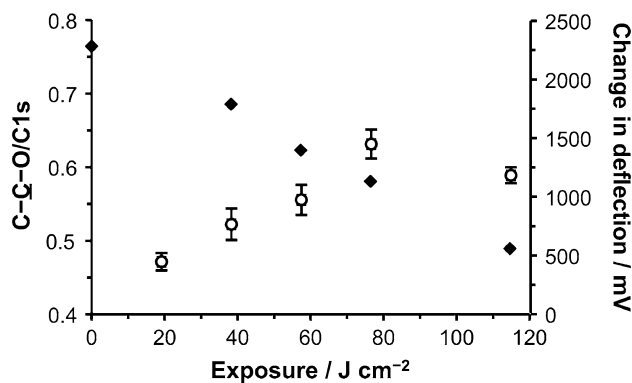


**Fig. 4** Variation in the relative area of the ether component of the C1s spectrum (*filled symbols*) and the difference in the lateral photodetector response between the masked and exposed areas (*open symbols*) with exposure

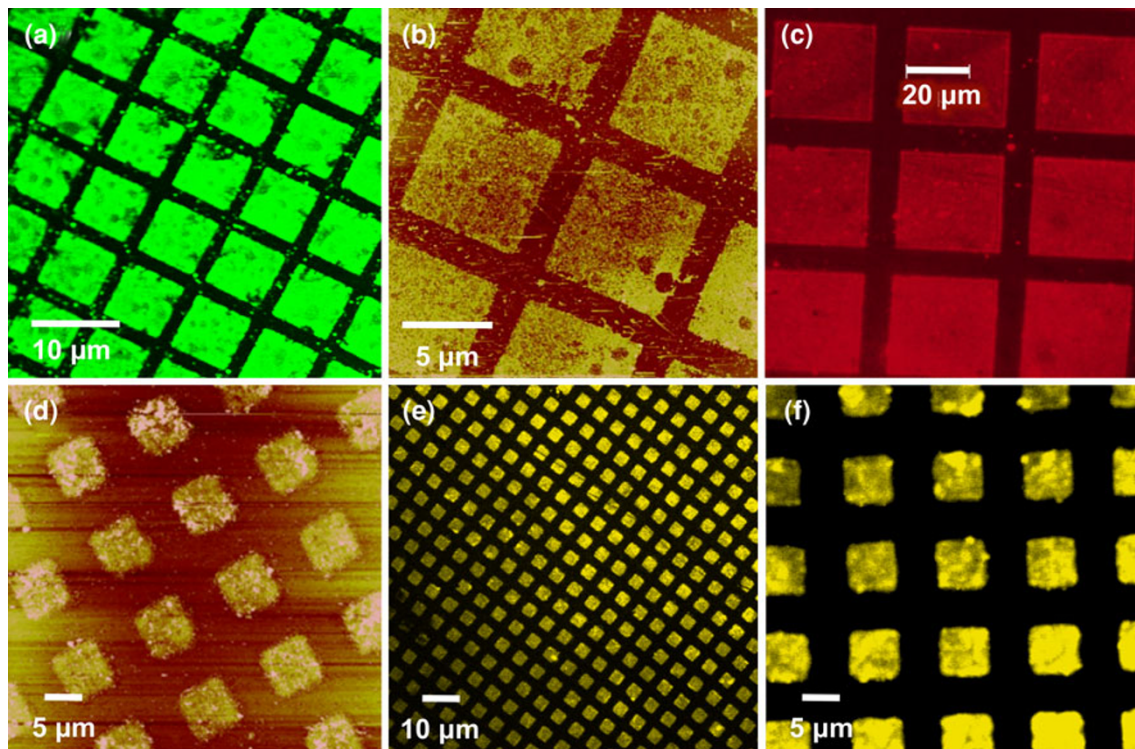


**Fig. 5** **a** Fluorescence microscopy image of a photopatterned OEG-silane film following immersion in a solution of Neutravidin nanoparticles. **b** Tapping mode AFM topographical image of a sample similar to the one shown in **a**. z-scale range (dark to bright) 0–60 nm. **c** Fluorescence micrograph of a photodegraded OEG-silane film following immersion in a solution of Alexa fluor 532-labeled

streptavidin. **d** Tapping mode AFM topographical image of a pattern formed by UV exposure through a mask, followed by attachment of AB-NTA, complexation with  $\text{Ni}^{2+}$  and incubation in a solution of His-tagged YFP. **e**, **f** Confocal fluorescence microscopy images of similar samples to the one shown in **d**

fluorescence is observed from the regions of the surface previously exposed to UV light (the squares), while the masked regions exhibit dark contrast.

Photodegradation of the OEG chains leads to the introduction of aldehyde groups, albeit at low density. These may be exploited to enable site-specific binding of proteins. Following exposure, samples were immersed in a solution of aminobutyl nitrilotriacetic acid (AB-NTA). The amine group of the aminobutyl linker reacts with aldehydes at pH 5 to form an imine bond. Subsequent complexation of NTA with  $\text{Ni}^{2+}$  yields a surface that can bind histidine-labeled proteins strongly. Figure 5d shows a tapping mode AFM topographical image of a sample treated in this way, following incubation in a solution of His-tagged YFP. The protein has attached densely to the exposed regions (squares), but not to the areas that were masked during exposure (bars). The strong intrinsic fluorescence of YFP enables the patterns to be characterized by confocal microscopy. Fluorescence images (Fig. 5e, f) exhibited bright fluorescence from exposed regions, and dark contrast in the masked areas, confirming the spatial selectivity of the adsorption of the protein.

OEG-silane films were exposed to UV light in a Lloyd's mirror interferometer, with the angle  $2\theta$  between the mirror and sample set to  $90^\circ$ , and characterized using FFM. Figure 6a shows an image of a  $20 \times 20 \mu\text{m}^2$  region of a sample that has been exposed for 6 min with a laser power of  $50 \text{ mW cm}^{-2}$ . Even at comparatively low magnification, long bands of alternative bright and dark intensity are evident. The lines cover the image area uniformly and there are few defects (the small dark globular feature probably represents surface contamination rather than infidelity in the interferogram). The high degree of pattern uniformity seen here was observed across an area that was 8 mm in diameter. Figure 6b shows a high magnification image of the region identified with a box in Fig. 6a. The alternating bands of bright and dark intensity may be observed clearly. The dark contrast corresponds to unmodified regions of the surface, while the bright intensity corresponds to regions, where significant modification of the surface has occurred. The Lloyd's mirror interferometer yields a sinusoidal pattern of intensity, and hence, the modification of the surface only approaches zero at the minima in the interference pattern. The widths of the broad bands in Fig. 6b were ca.



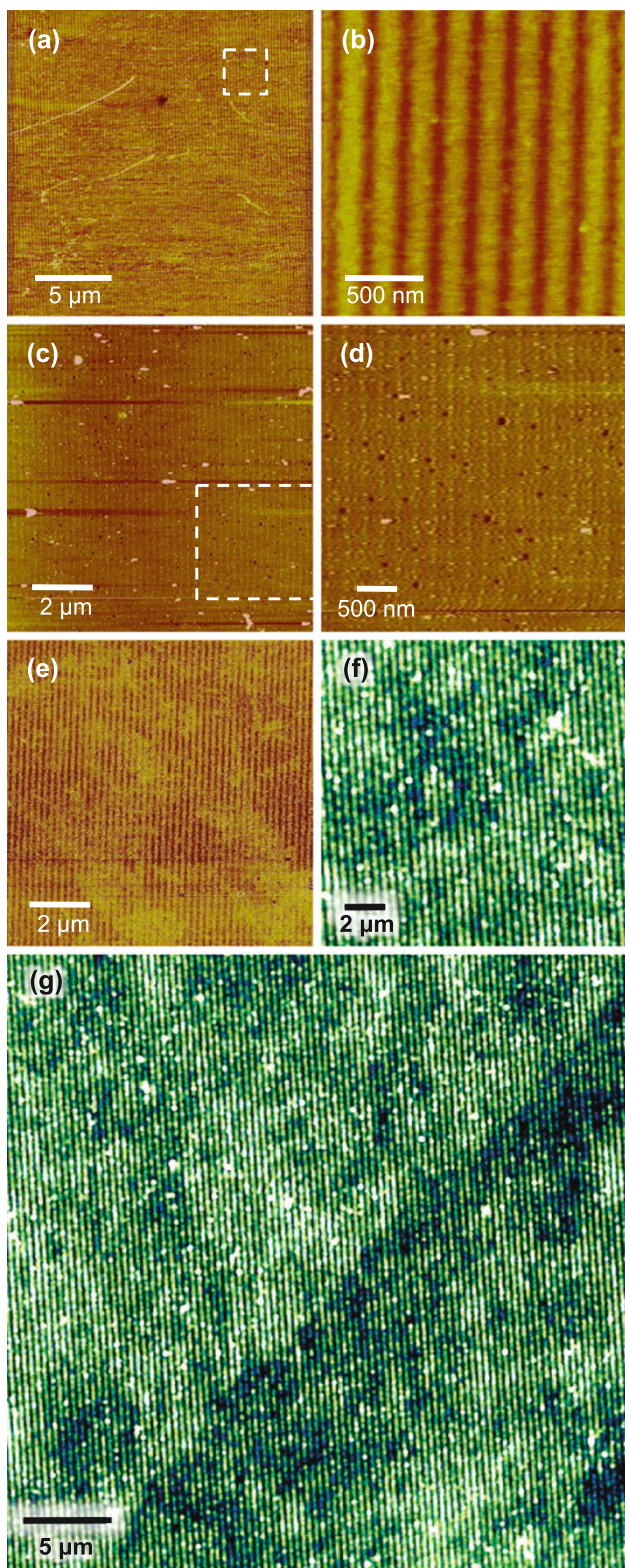


**Fig. 6** Images of nanopatterns formed by interferometric exposure of monolayers of OEG-silane on glass. **a, b** FFM images of a sample exposed for 6 min at  $50 \text{ mW cm}^{-2}$ . **c, d** Tapping mode AFM topographical images of similar samples to those in **a** and **b**, following immersion in a solution of streptavidin in PBS. **e** Tapping mode phase image of a sample exposed at the same power for 10 min following adsorption of streptavidin. Image size:  $10 \times 10 \mu\text{m}^2$ , z-contrast range 0–50° dark to bright. **f, g** Confocal fluorescence microscopy images of two regions of a sample formed by interferometric exposure of an OEG-silane film with  $2\theta = 20^\circ$ , NTA functionalization,  $\text{Ni}^{2+}$  complexation, and incubation in a solution of His-tagged GFP

following immersion in a solution of streptavidin ( $1 \mu\text{g mL}^{-1}$ ) in phosphate buffered saline for 30 min. Even at comparatively low magnification, fine lines of protein may be observed running vertically down the imaged region. Small bright features observed to be distributed randomly across the sample surface are attributed to salt crystals (samples exposed to buffer solutions often exhibit small amounts of particulate matter, likely due to deposition of ions from the buffer). Figure 6d shows the region marked with a box in Fig. 6c at higher magnification. The lines of adsorbed protein are much more clearly evident. The FWHM of the protein lines was only 30 nm, ca.  $\lambda/8$  and substantially smaller than the period and the FWHM of the interference pattern. A small number of dark features are observed in Fig. 6d; these are attributed to defects in the siloxane film.

The observation of such narrow protein lines is surprising, given the comparatively broad features that were observed by FFM prior to immersion of the sample in the protein solution. FFM measures changes in surface friction that are probably attributable to changes in the mode of adsorbate conformational deformation under loading through the AFM probe; the FFM images do not measure the adhesiveness of the surface toward protein adsorption. The most likely explanation for the observation of such narrow protein features in Fig. 6d is that while the interferometric exposure causes degradation of the OEG terminal groups over a linear region area some 200 nm wide (and macroscopic in length), the greater part of the exposed area remains resistant to protein adsorption, probably, because only a small number of OEG groups have been removed. The low degree of order in the siloxane film, and the comparatively lengthy OEG chain used here (6–9 ethylene glycol monomers), confer sufficient conformational freedom for intact chains to cover defects induced by photodegradation and protein-binding aldehyde functional groups, except in the areas that have been exposed to the highest intensities of UV irradiation, close to the maxima in the interference pattern. We conclude that there is a threshold dose above which the OEG-silane film becomes adhesive toward proteins, conferring an additional degree of control in the nanopatterning process and enabling the

200 nm, with the dark bands separating them having widths of ca. 70 nm.

Figure 6c shows a tapping mode AFM topographical image of a sample similar to that shown in Fig. 6a, b

fabrication of structures significantly smaller than one half the period of the interference pattern.

An increase in the exposure time from 6 to 10 min ( $18\text{--}30\text{ J cm}^{-2}$ ) yielded an increase in the FWHM of the streptavidin structures from 30 to 90 nm (Fig. 6e). The substantial increase in line width accompanying this modest increase in exposure supports the hypothesis above, that an effective non-linearity is produced in the process by the existence of a “threshold” density of ethylene glycol units at which protein-resistance is lost. From Fig. 6c, d, we conclude that much of the surface has received an exposure below that required to exceed the threshold, while in Fig. 6e a much larger fraction of the surface has received adequate exposure for protein-resistance to be lost.

Finally, nanopatterning was also combined with site-specific immobilization. In order to enable subsequent characterization of the samples using fluorescence microscopy, the angle between the sample and mirror was adjusted to  $20^\circ$ , increasing the period to 340 nm. After exposure to a dose of  $58\text{ J cm}^{-2}$ , the sample was derivatized with AB-NTA, and complexed with  $\text{Ni}^{2+}$ , following the same procedure used to prepare the samples shown in Fig. 5d–f. The sample was then incubated in a solution of His-tagged GFP for 20 h. Despite the small period, the nanoscopic lines are clearly evident in Fig. 6f. The protein features appear broadened, because the line width (ca. 170 nm) is smaller than the resolution limit of the microscope. However, the contrast difference is clear.

Previously, interferometric methods were applied without success to the patterning of poly(oligoethylene methacrylate) polymer brushes by UV degradation. The success in the present case is attributed to the much thinner resist used. However, the slower rate of modification may also be important in the present case, because the more rapidly modified polymer brushes are apt to become more easily over-exposed, leading to broader protein-adhesive bands.

The principal drawback to the methodology described here is the comparatively slow rate of modification of the siloxane film, as reflected, for example, in the XPS data in Fig. 2. Moreover, to yield the narrowest protein structures, the exposure time must be finely judged to avoid either causing too little modification for extensive protein adsorption or causing modification over a broader region (ca. 90 nm for sample and mirror set at right-angles). However, the simplicity of the process is very attractive, and the capacity to fabricate protein nanopatterns over a macroscopic area, on a convenient substrate such as glass, is extremely attractive for fundamental studies of biological behavior at interfaces. The protein-resistance of the unmodified OEG-silane films seems to be extremely good, yielding extremely clear fluorescence contrast even for a protein like YFP, with a high level of intrinsic fluorescence. The simple process described here offers significant

scope for adaptation in future work to enable the construction of more complex nanostructured assemblies of biomolecules.

## 4 Conclusions

Exposure of films formed by the adsorption of OEG terminated silanes onto glass may be photodegraded by exposure to UV light with a wavelength of 244 nm. The ether component in the C1s spectrum and the total amount of carbon in the film both decrease with exposure. A small aldehyde peak is observed in the C1s region after UV modification. The coefficient of friction, measured by FFM, was found to increase following UV exposure. The rate of change is significantly slower than is observed for OEG terminated monolayers on gold. However, patterning may be accomplished easily by exposing samples to UV light through a mask. Fluorescence microscopy data demonstrate that proteins adsorb non-specifically to exposed regions, but not to unmodified regions providing a simple one-step route to the creation of protein micropatterns. Attachment of NTA, by imine bond formation from an amine linker to the exposed regions, enables site-specific attachment of His-tagged proteins. Using a Lloyd’s mirror interferometer, it was possible to fabricate nanopatterns over an area 8 mm in diameter with a high degree of perfection in a simple, rapid process. As an example, 30-nm wide ( $\lambda/8$ ) lines of streptavidin were formed by immersion of the samples in a solution of the protein.

**Acknowledgments** GT, DGL, and GJL thank EPSRC (grants EP/D064767/1 and GR/C523857/1) for financial support. GJL, SP, and CNH gratefully acknowledge financial support from the Biotechnology and Biological Sciences Research Council (BBSRC). OEZ thanks the Libyan Government for a Research Scholarship. GPL thanks the Office of Naval Research (Grant no. N00014-10-1-0907) and the National Science Foundation, Research Triangle MRSEC (Grant no. DMR-1121107) for financial support. The Wellcome Trust (Grant Nos. GR077544AIA and WT093134MA) is thanked for support of the Sheffield Light Microscopy Facility.

**Open Access** This article is distributed under the terms of the Creative Commons Attribution License which permits any use, distribution, and reproduction in any medium, provided the original author(s) and the source are credited.

## References

1. Lopez GP, Albers MW, Schreiber SL, Carroll R, Peralta E, Whitesides GM (1993) *J Am Chem Soc* 115:5877–5878
2. Lopez GP, Biebuyck HA, Haerter R, Kumar A, Whitesides GM (1993) *J Am Chem Soc* 115:10774–10781
3. Singhvi R, Kumar A, Lopez GP, Stephanopoulos GN, Wang DIC, Whitesides GM, Ingber DE (1994) *Science* 264:696–698



4. Scotchford CA, Cooper E, Downes S, Leggett GJ (1998) *J Biomed Mater Res* 41:431–442
5. Lee K-B, Park S-J, Mirkin CA, Smith JC, Mrksich M (2002) *Science* 295:1702–1705
6. DeMond AL, Mossman KD, Starr T, Dustin ML, Groves JT (2008) *Biophys J* 94:3286–3292
7. Hartman NC, Nye JA, Groves JT (2009) *Proc Natl Acad Sci USA* 106:12729–12734
8. Lee K-B, Lim J-H, Mirkin CA (2003) *J Am Chem Soc* 125:5588–5589
9. Anker JN, Hall WP, Lyandres O, Shah NC, Zhao J, Van Duyne RP (2008) *Nat Mater* 7:442–453
10. Ferreira J, Santos MJL, Rahman MM, Brolo AG, Gordon R, Sinton D, Girotto EM (2008) *J Am Chem Soc* 131:436–437
11. Demers L, Ginger DS, Park S-J, Li Z, Chung S-W, Mirkin CA (2002) *Science* 296:1836–1838
12. Liu M, Amro NA, Chow CS, Liu G-Y (2002) *Nano Lett* 2:863–867
13. Chow DC, Lee W-K, Zauscher S, Chilkoti A (2005) *J Am Chem Soc* 127:14122–14123
14. Falconnet D, Koenig A, Assi F, Textor M (2004) *Adv Funct Mater* 14:749–756
15. Agheli H, Malmstrom J, Larsson EM, Textor M, Sutherland DS (2006) *Nano Lett* 6:1165–1171
16. Calvacanti-Adam AE, Micoulet A, Blümmel J, Auernheimer J, Kessler H, Spatz JP (2006) *Eur J Cell Biol* 85:219–224
17. Coyer SR, García AJ, Delamar E (2007) *Angew Chem Int Ed* 46:6837–6840
18. Montague M, Ducker RE, Chong KSL, Manning RJ, Rutten FJM, Davies MC, Leggett GJ (2007) *Langmuir* 23:7328–7337
19. Reynolds NP, Janusz SJ, Escalante-Marun M, Timney J, Ducker RE, Olsen JD, Otto C, Subramanian V, Leggett GJ, Hunter CN (2007) *J Am Chem Soc* 129:14625–14631
20. Reynolds NP, Tucker JD, Davison PA, Timney JA, Hunter CN, Leggett GJ (2009) *J Am Chem Soc* 131:896–897
21. Falconnet D, Pasqui D, Park S, Eckert R, Schiff H, Gobrecht J, Barbucci R, Textor M (2004) *Nano Lett* 4:1909–1914
22. Liu G-Y, Amro NA (2002) *Proc Natl Acad Sci USA* 99:5165–5170
23. Wadu-Mesthrige K, Amro NA, Garno JC, Xu S, Liu G-Y (2001) *Biophys J* 80:1891–1899
24. Harris JM (1992) *Poly (ethylene glycol) chemistry: biochemical and biomedical applications*. Plenum, New York
25. Prime KL, Whitesides GM (1991) *Science* 252:1164–1167
26. Pale-Grosdemange C, Simon ES, Prime KL, Whitesides GM (1991) *J Am Chem Soc* 113:12–20
27. Ostuni E, Chapman RG, Holmlin ER, Takayama S, Whitesides GM (2001) *Langmuir* 17:5605–5620
28. Ma H, Li D, Sheng X, Zhao B, Chilkoti A (2006) *Langmuir* 22:3751–3756
29. Ma H, Textor M, Clark RL, Chilkoti A (2006) *Biointerphases* 1:35–39
30. Ma H, Wells M, Beebe Jr. TP, Chilkoti A (2006) *Adv Funct Mater* 16:640–648
31. López GP, Ratner BD, Tidwell C, Haycox C, Rapoza R, Horbett T (1991) *J Biomed Mater Res* 26:415
32. Iwasaki Y, Kurita K, Ishihara K, Nakabayashi N (1997) *J Biomater Sci Polym Ed* 8:151–163
33. Kyomoto M, Iwasaki Y, Moro T, Konno T, Miyaji F, Kawaguchi H, Takatori Y, Nakamura K, Ishihara K (2007) *Biomaterials* 28:3121–3130
34. Nakabayashi N, Williams DF (2003) *Biomaterials* 24:2431–2435
35. Lewis AL (2000) *Colloids Surf B* 18:261–275
36. Ducker RE, Janusz SJ, Sun S, Leggett GJ (2007) *J Am Chem Soc* 129:14842–14843
37. Alang Ahmad SA, Wong LS, ul-Haq E, Hobbs JK, Leggett GJ, Micklefield J (2011) *J Am Chem Soc* 133:2749–2759
38. Ballav N, Terfort A, Zharnikov M (2009) *Langmuir* 25:9189–9196
39. Ballav N, Thomas H, Winkler T, Terfort A, Zharnikov M (2009) *Angew Chem Int Ed* 48:5833–5836
40. Golzhauser A, Eck W, Geyer W, Stadler V, Grunze M (2001) *Adv Mater* 13:806
41. Hurley CR, Ducker RE, Leggett GJ, Ratner BD (2010) *Langmuir* 26:10203–10209
42. Alang-Ahmad SA, Hucknall A, Chilkoti A, Leggett GJ (2010) *Langmuir* 26:9937–9942
43. Jeyachandran YL, Terfort A, Zharnikov M (2012) *J Phys Chem C* 116:9019–9028
44. Shah SS, Howland MC, Chen L-J, Silangcruz J, Verkhoturov SV, Schweikert EA, Parikh AN, Revzin A (2009) *ACS Appl Mater Interfaces* 1:2592–2601
45. Brueck SRJ (2005) *Proc IEEE* 93:1704–1721
46. Lu C, Lipson RH (2009) *Laser Photon Rev* 1–13
47. Turchanin A, Schnietz M, El-Desawy M, Solak HH, David C, Golzhauser A (2007) *Small* 3:2114–2119
48. Schuh C, Santer S, Prucker O, Ruhe J (2009) *Adv Mater* 21:4706–4710
49. Kremers G-J, Munster EBv, Goedhart J, Gadella TWJ (2007) *Biophys J* 92:3775–3783
50. Adams J, Tizazu G, Janusz S, Brueck SRJ, Lopez GP, Leggett GJ (2010) *Langmuir* 26:13600–13606
51. Huang J, Hemminger JC (1993) *J Am Chem Soc* 115:2243–3343
52. Brewer NJ, Janusz SJ, Critchley K, Evans SD, Leggett GJ (2005) *J Phys Chem B* 109:11247–11256
53. Shah SS, Lee JY, Verkhoturov S, Tuleuova N, Schweikert EA, Ramanculov E, Revzin A (2008) *Langmuir* 24:6837–6844